Cancer Diagnostics

Deutsche Ausgabe: DOI: 10.1002/ange.201503067
Internationale Ausgabe: DOI: 10.1002/anie.201503067

Tracking Cancer Metastasis In Vivo by Using an Iridium-Based Hypoxia-Activated Optical Oxygen Nanosensor**

*Xianchuang Zheng, Huang Tang, Chen Xie, Jialiang Zhang, Wei Wu, and Xiqun Jiang**

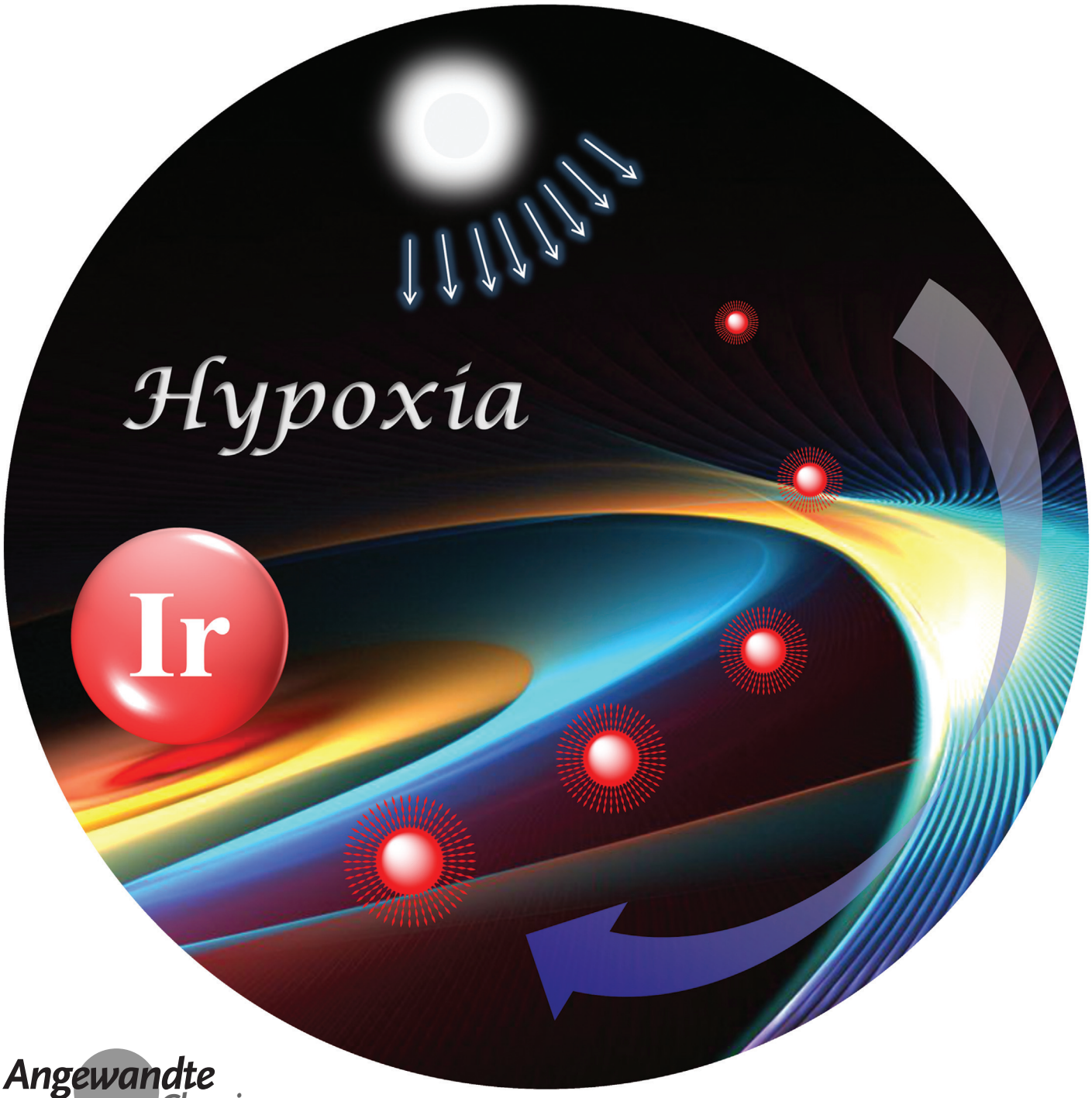

Abstract: *We have developed a nanosensor for tracking cancer metastasis by noninvasive real-time whole-body optical imaging. The nanosensor is prepared by the formation of co-micelles from a poly(N-vinylpyrrolidone)-conjugated iridium-(III) complex (Ir-PVP) and poly(ε-caprolactone)-b-poly(N-vinylpyrrolidone) (PCL-PVP). The near-infrared phosphorescence emission of the nanosensor could be selectively activated in the hypoxic microenvironment induced by cancer cells. The detection ability of the nanosensor was examined in cells and different animal models. After intravenous injection, the nanosensor can be effectively delivered to the lung and lymph node, and cancer cell metastasis through bloodstream or lymphatics can be quickly detected with high signal-to-background ratio by whole-body imaging and organ imaging. Moreover, the nanosensor exhibits good biocompatibility both in vitro and in vivo. The nanosensor is believed to be a powerful tool for the diagnosis of cancer metastasis.*

Although surgical treatment and adjuvant therapy have proven effective to control primary tumors, cancer metastasis still suffers from poor prognosis and has become the primary cause of death of most cancer patients.[1] At present, accurate diagnosis of cancer metastasis is challenging. Optical imaging is a promising method for cancer diagnosis, as it can provide real-time information about cancer metastasis non-invasively and is inexpensive. So far, many works on optical imaging of cancer metastasis rely on labeling cancer cells beforehand with luciferase or fluorescent tags, such as green fluorescent protein (GFP) and quantum dots.[2] However, this is not practical for real diagnosing circumstances. Therefore, developing extrinsic optical sensors that can specifically report cancer cell metastasis after systemic administration will be very meaningful.

Hypoxia is a characteristic feature for most solid tumors due to the imbalance between the cancer cell proliferation and limited oxygen supply from blood vessels.[3] Hypoxia-inducible factor 1α (HIF-1α) is found to play a crucial role in tumor metastasis.[4] Hypoxia-targeted probes, such as nitroimidazole and Cu^{II} diacetylbis(N4-methylthiosemicarbazone) (Cu-ATSM), have been widely used in cancer diagnosis.[5] Recently, hypoxia-sensitive phosphorescent transition metal complexes are emerging as new tumor imaging agents with significantly higher sensitivity and specificity.[6] Some studies were reported on the detection of primary tumors by using hypoxia-sensitive probes;[7] for example, dendrimer-based Pd^{II}/Pt^{II} porphyrins have shown effective tumor imaging ability.[8] However, employing a hypoxia-sensitive imaging probe for tracking cancer metastasis in vivo is less explored.

Here we report a hypoxia-specific macromolecular probe based on a poly(*N*-vinylpyrrolidone)-conjugated iridium (III) complex for the detection of tumors and cancer cells in vivo.[9] On this basis, we have developed a hypoxia-sensitive optical nanosensor for tracking cancer metastasis in vivo. The nanosensor (named Ir-CM) was prepared by the formation of co-micelles based on a poly(*N*-vinylpyrrolidone) ($M_n = 13\,000$)-conjugated iridium (III) complex (Ir-PVP) and poly(ε-caprolactone)-*b*-poly(*N*-vinylpyrrolidone) (PCL-PVP, $M_{nPCL} = 5$k, $M_{nPVP} = 12\,000$) (Figure 1a). The hydrophobic PCL block and the Ir complex moiety constitute the core of the micelle, hydrophilic PVP chains form the shell.

An transmission electron microscopy (TEM) image shows that the nanosensor has a near-spherical shape with a diameter of around 30 nm in its dry state (Figure 1b). In aqueous solution, Ir-CM has a mean hydrodynamic diameter of 49.7 nm with narrow size distribution as measured by dynamic light scattering (DLS) (Figure 1c). The zeta potential of Ir-CM is determined to -11.24 ± 1.53 mV in PBS (pH 7.4). Ir-CM exhibits remarkable stability without significant size change in PBS and fetal bovine serum buffer for 7 days

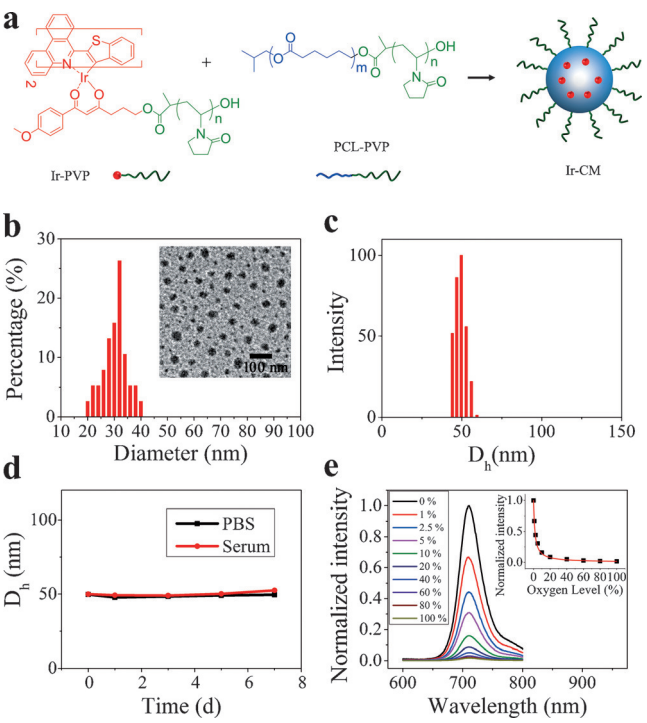

Figure 1. a) Synthesis of Ir-CM. The molar ratio of PCL-PVP and Ir-PVP is 4:1. b) TEM image of Ir-CM (insert) and particle size distribution in the TEM image. c) DLS analysis of Ir-CM in distilled water. d) Stability assessment of Ir-CM. Ir-CM was diluted with PBS (1×) or fetal bovine serum buffer (serum/PBS 1:1) for one-fold. Then the hydrodynamic diameter of the diluted co-micelle solution was measured after it was stored at room temperature for different time (0 to 7 days). e) Phosphorescence emission spectra of Ir-CM in distilled water at different oxygen levels. Excitation: 560 nm. Insert: Decay curve of peak intensities of Ir-CM with increasing oxygen level.

[*] X. C. Zheng, H. Tang, C. Xie, J. L. Zhang, Prof. W. Wu, Prof. X. Q. Jiang
MOE Key Laboratory of High Performance Polymer Materials and Technology, Collaborative Innovation Center of Chemistry for Life Sciences, and Department of Polymer Science & Engineering, College of Chemistry & Chemical Engineering, Nanjing University
Nanjing, 210093 (P. R. China)
E-mail: jiangx@nju.edu.cn

[**] This work was supported by the Natural Science Foundation of China (No. 51033002, 21474045, and 51273090), the Specialized Research Fund for the Doctoral Program of Higher Education, and the Program for Changjiang Scholars and Innovative Research Team in University.

Supporting information for this article is available on the WWW under http://dx.doi.org/10.1002/anie.201503067.

(Figure 1d). Photophysical analysis reveals that Ir-CM has a near-infrared emission at 710 nm and a broad absorption band in the visible range with an absorption peak at 560 nm (Figure 1e and Figure S1 in the Supporting Information). The quantum yield of Ir-CM is determined to be 0.10 in Ar-saturated aqueous solution. The phosphorescence emission of Ir-CM increases sharply with the decrease of oxygen level and the sensitivity is high enough to distinguish hypoxic (< 3% O_2) and normoxic conditions (Figure 1e). There is a 60-fold increase in phosphorescent emission intensity from oxygen-saturated condition to oxygen-free condition, demonstrating that Ir-CM can function as an effective agent for hypoxia-activated imaging. Compared to other recently reported oxygen sensors based on nanoparticles or films loaded with Ir^{III}, Ru^{II}, Pd^{II} or Pt^{II} complexes (Table S1), the merits of Ir-CM are its high oxygen sensitivity and improved excitation and emission wavelength while the reported sensors have other advantages such as ratiometric imaging and two-photon excitation.[10] Compared with small molecular Ir^{III} complex sensors,[11] nanoscale Ir-CM should have high cellular uptake and passive targeting abilities toward tumors, as well as reduced interference from other biomolecules in oxygen sensing. These advantages make Ir-CM more suitable for hypoxia imaging in cells and tumors.

We first evaluated the hypoxia response behavior of the nanosensor in monolayer cell cultures in vitro. As shown in Figure 2a, Ir-CM is effectively taken up by human neuroblastoma SH-SY5Y cells into the cytoplasm after incubation for 2 h. The cells treated with Ir-CM (0.3 mg mL^{-1}) exhibited intense phosphorescent emission signal only under hypoxic condition (0%), while the signal was quite weak under higher oxygen conditions (10% and 21%). The change in signal intensity positively correlates to the HIF-1α expression and pimonidazole (commercial hypoxia probe)-staining level of the cells (Figure 2b). Strong phosphorescence emission of the nanosensor is accompanied by high HIF-1α expression and high pimonidazole staining. The results show the high hypoxia dependence of the phosphorescence emission of Ir-CM after cellular uptake. Similar cell uptake and hypoxia response behavior were also found in murine hepatocarcinoma H22 cells (Figure 2c). The three-dimensional multicellular spheroid has a hypoxic microenvironment in its interior due to limited oxygen diffusion.[12] SH-SY5Y multicellular spheroids were employed to evaluate the hypoxia response of Ir-CM. As shown in Figure 2d, after treatment with Ir-CM (0.3 mg mL^{-1} for 8 h) a strong phosphorescent emission signal is detected from the hypoxic interior rather than the periphery exposed to the atmosphere and culture medium, indicating the high specificity of the nanosensor to hypoxia.

Next, we focused on the detection of cancer cell metastasis in vivo by using Ir-CM. H22 cells (10^6) were injected in the tail vein of ICR mice to establish a lung metastasis model through the bloodstream. After 7 days the metastases-bearing mice were intravenously injected with Ir-CM (100 mg kg^{-1}) and observed in the in vivo imaging system. At 1 h after injection of Ir-CM, a strong phosphorescence signal was detected in the lung with very low nonspecific background signals (Figure 3a). At 24 h and 48 h after injection, the strong signal was still maintained in the lung sites (Figure S2). Ex vivo examination of the mice's lung tissue revealed the appearance of many cancer cell metastases in the lung (Figure 3b). Ex vivo imaging of various organs dissected from the mice at 48 h after injection of Ir-CM, including heart, liver, kidney, metastases-bearing lung, brain and spleen, confirmed that the exclusive phosphorescent emission signal seen in the whole-body imaging came from the metastases-bearing lung (Figure 3c). The signal intensity from the metastases-bearing lung was more than 6-fold stronger than from other organs at 48 h after injection of Ir-CM (Figure 3d). To figure out the nanosensor's detection mechanism for lung metastasis, further assessment of the biodistribution of Ir-CM in the whole body of metastases-bearing mice at different time-points after intravenous injection was performed. The data of Ir-CM distribution are expressed as percentage of injected dose per gram of tissue (ID/g) at each test point. As shown in Figure 3e, Ir-CM was found to mainly accumulate in the reticuloendothelial system (RES)-rich organs such as spleen and liver. The blood half-life of Ir-CM was calculated to 1.7 h. At 48 h post-injection, the mean concentration of Ir-CM was 4.1% ID/g in the lung with metastases, lower than the 11.0% ID/g in the spleen and comparable with the 4.0% ID/g in the liver. By combining the results of the signal intensities and concentrations of Ir-CM in various organs, it was concluded that, in contrast to other hypoxia-targeted probes such as nitroimidazole and Cu-ATSM, the detection of lung metastases with low nonspecific background signals is not based on the accumulation effect of the nanosensor.[5] Instead, the detection is mainly attributed to the selective enhancement of the phosphorescent emission signal of Ir-CM in the hypoxic lung metastases due to its hypoxia-activated feature. The remarkably hypoxic microenvironment of metastases-bearing lung was confirmed by a strong HIF-1α and pimonidazole staining in frozen sections (Figure 3f and g). Moreover, the metastases-bearing lung

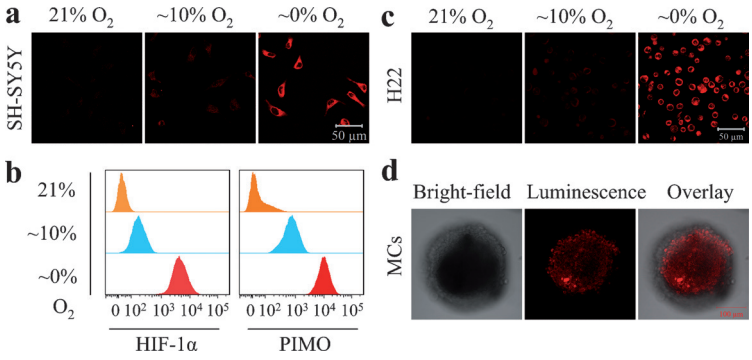

Figure 2. a) Confocal luminescence images of SH-SY5Y cells after treatment with Ir-CM and incubation at different oxygen levels. b) SH-SY5Y cells were stained with HIF-1α antibody and pimonidazole (PIMO) antibody after incubation at different oxygen levels. The staining levels of HIF-1α antibody and pimonidazole antibody were measured with a flow cytometer. c) Confocal luminescence images of H22 cells after treatment with Ir-CM and incubation at different oxygen levels. d) Confocal luminescence images of SH-SY5Y multicellular spheroids (MCs) after incubation with Ir-CM for 8 h.

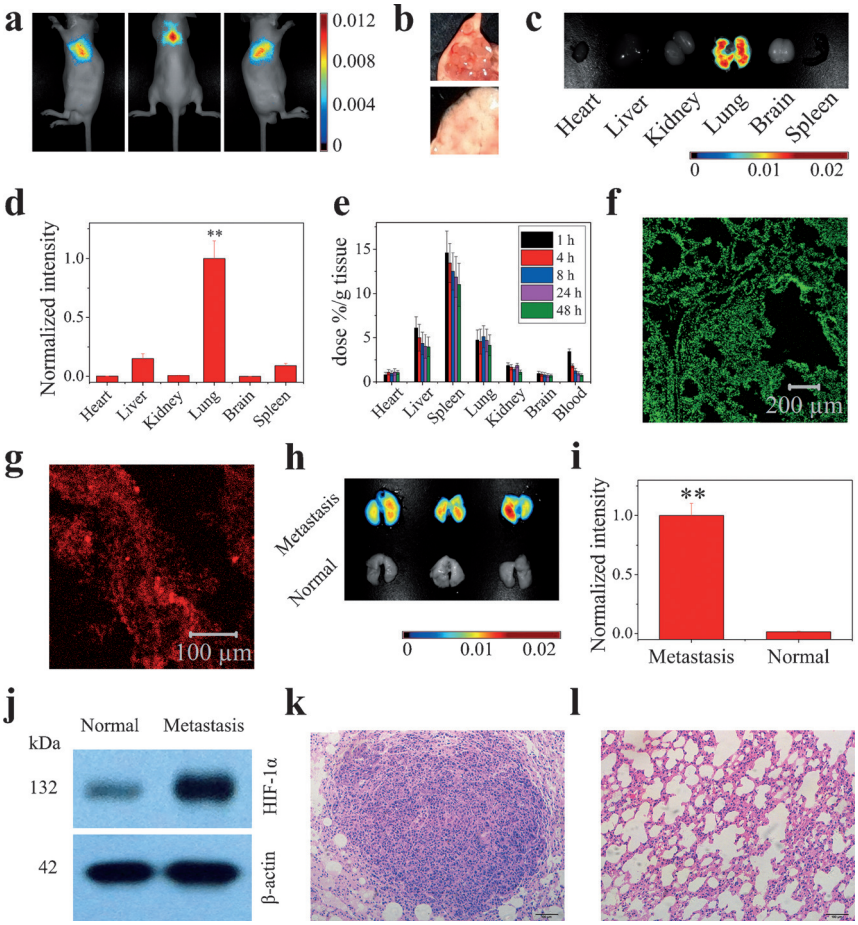

Figure 3. a) Whole-body optical imaging of ICR mice bearing lung metastases from three different angles at 1 h after injection. b) Bright-field images of lung with metastases (above) and normal lung (below). c) Ex vivo images of different organs dissected from ICR mice bearing lung metastases. d) Signal intensities detected from different organs ($n=5$). $^{**}P<0.01$, in comparison between the signal intensities from the metastases-bearing lung and other normal organs by a one-way analysis of variance (ANOVA). e) Biodistribution assay of Ir-CM in different organs and blood of ICR mice bearing lung metastases. f,g) Frozen sections of the metastases-bearing lung after staining with HIF-1α antibody (f) and pimonidazole antibody (g). h) Ex vivo images of lungs dissected from ICR mice bearing lung metastases and normal ICR mice ($n=3$ per group). i) Comparison of the signal intensities of the lung metastases group and normal lung group in (h). $^{**}P<0.01$, in comparison between the signal intensities of the two groups by a two-sample Student t-test. j) Western blots of HIF-1α expression in the normal lung and metastases-bearing lung. k,l) H&E stained slices of metastases-bearing lung (k) and normal lung (l). Scale bar: 100 μm.

exhibited a much stronger phosphorescent signal than a normal lung (Figure 3h). At 48 h post-injection, the signal intensity of the metastases-bearing lung was about 60-fold stronger than that of the normal lung (Figure 3i). It was also found that there is no severe difference between the Ir-CM concentrations in the metastases-bearing and normal lung (Figure S3). The Ir-CM concentration was 4.1% ID/g in metastases-bearing lung and 3.6% ID/g in normal lung at 48 h post-injection. Western blotting showed that the HIF-1α expression level was much higher in the metastases-bearing lung than in the normal lung (Figure 3j). Accumulation of cancer cells in the metastases-bearing lung was confirmed by histological examination (Figure 3k and l). These results indicate that Ir-CM has high specificity to metastases-bearing over normal lung, based on the selective enhancement of the phosphorescent signal by the hypoxic microenvironment in metastatic cancer cells. Therefore, by using Ir-CM the metastasis of cancer cells to lung through the bloodstream can be accurately detected with high signal-to-background ratio.

As fatal lung metastasis often results in the quick death of cancer patients, diagnosis of cancer lung metastasis by optical imaging is of great importance for cancer treatment. To our best knowledge, Ir-CM is the first hypoxia-activated optical nanosenor that has been applied in the detection of lung metastasis in vivo. As the lung is the organ with the highest oxygen level (about 14–20% O_2) in the body, the hypoxia-activated nanosensor located in the normal lung will yield a very low nonspecific signal. Thus it should be a very promising method to employ a hypoxia-activated nanosensor for the detection of lung metastasis.

Besides metastasis through the blood stream, lymphatics are another major metastasis route for cancer cells. H22 cells were subcutaneously implanted to the right rear paw of ICR mice to establish a lymph node metastasis model. After 20 days the mice were intravenously injected with Ir-CM (100 mg kg^{-1}) and imaged. At 1 h after injection of Ir-CM, phosphorescent signals were detected from two regions of the mice by whole-body optical imaging (Figure 4a). One corresponded to the primary tumor in the right rear paw and another was located in the right groin. Imaging after removal of local skin confirmed that the second signal came from the right inguinal lymph node (Figure 4b). By comparison between the right inguinal lymph nodes from the metastases-bearing mice and normal mice at 1 h after injection of Ir-CM, it was found that only metastatic lymph nodes exhibited strong phosphorescent signals, while the signals from normal lymph nodes were very weak (Figure 4c). The phosphorescent signals detected from the metastatic lymph nodes were about 30-fold stronger than that detected from normal lymph nodes at 1 h post-injection (Figure 4d). It was also found that the metastatic lymph nodes were significantly swollen to about 8-times in weight as compared to the normal lymph nodes (Figure S4), which is ascribed to the accumulation of a large amount of cancer cells in the metastatic lymph node as observed in the histological examination (Figure 4e and f). On the other hand, RT-PCR assessment demonstrated that the expression levels of HIF-1α

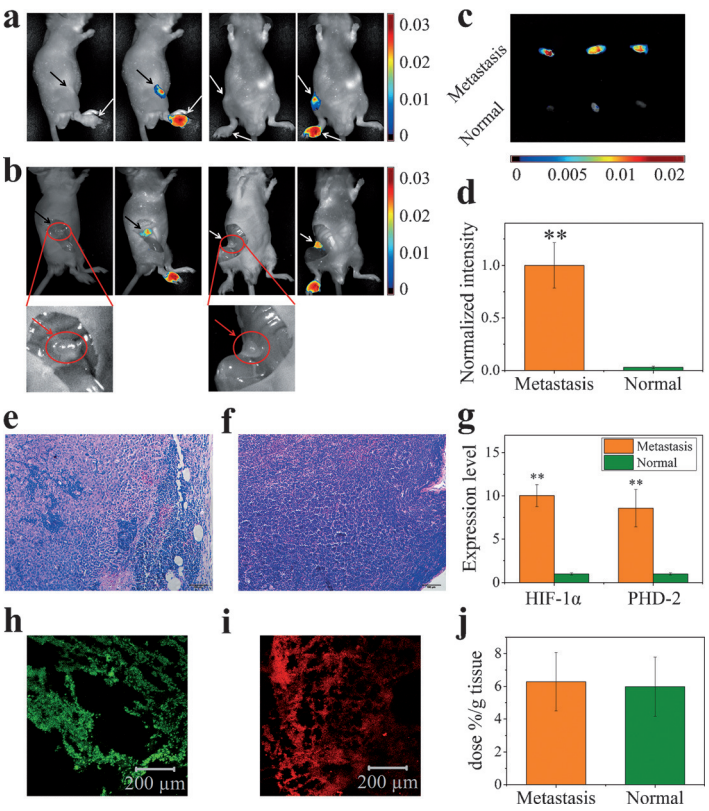

Figure 4. a) Whole-body optical imaging of ICR mice bearing H22 tumor in the right rear paw from two angles at 1 h post-injection. b) The mice were imaged again after removal of the local skin. The amplified white images reveal the location of the inguinal lymph node. c) Ex vivo images of the right inguinal lymph nodes from ICR mice bearing H22 tumor in the right rear paw and normal mice ($n=3$ per group). d) Comparison between the signal intensities of the metastatic right inguinal lymph node group and normal right inguinal lymph node group in (c). $^{**}P<0.01$, using a two-sample Student t-test. e,f) H&E stained slices of metastatic lymph node (e) and normal lymph node (f). Scale bar: 100 μm. g) The expression levels of HIF-1α mRNA and PHD-2 mRNA of metastatic and normal lymph nodes assayed by RT-PCR ($n=3$). $^{**}P<0.01$, using a two-sample Student t-test. h,i) Frozen sections of the metastatic lymph node were stained with HIF-1α antibody (h) and pimonidazole antibody (i). j) The concentration of Ir-CM in the metastatic and normal lymph nodes ($n=5$).

mRNA and prolylhydroxylase domain 2 (PHD-2) mRNA were about an order of magnitude higher in the metastatic lymph nodes than in the normal lymph nodes (Figure 4g), indicating the distinct hypoxic condition of metastatic lymph node over normal lymph node.[13] The hypoxic microenvironment of the metastatic lymph node was also verified by the strong HIF-1α and pimonidazole staining in frozen sections (Figure 4h and i). The Ir-CM concentrations in the metastatic and normal lymph nodes were found to be very similar (Figure 4j). The mean concentration of Ir-CM was 6.3 % ID/g in the metastatic lymph nodes versus 6.0 % ID/g in the normal lymph nodes at 1 h post-injection. As a result, the detection of lymph node metastasis is mainly based on the hypoxia-activation of the nanosensor under the hypoxic conditions induced by cancer cell accumulation. These results indicate that Ir-CM is not only feasible in the detection of primary tumors, but is also sufficiently sensitive to detect lymph node metastasis after systemic injection. In addition, it provides high specificity to distinguish metastatic from normal lymph nodes.

In spite of their great importance for the diagnosis of lymph node metastasis, the delivery of extrinsic imaging agents to the lymph nodes is often not straightforward. Nanomaterials with relatively large diameter (> 100 nm) have difficulties to reach the lymph node, while such with sizes less than 20 nm are often too small to be trapped in the lymph node.[14] The proper diameter for delivery to the lymph node has been found to be 20–50 nm.[15] A slightly negative surface charge and hydrophilic surface are also reported to be advantageous for lymph node accumulation.[16] Our nanosenor, Ir-CM, happens to possess all these advantages. A biodistribution assay shows a significant accumulation and retention of Ir-CM in the metastatic lymph node after intravenous injection (Figure S5). At 4 h post-injection, the mean concentration of Ir-CM in metastatic lymph node was 7.1 % ID/g, i.e. higher than its concentration in primary tumors (5.3 %/g tissue) and other normal organs (heart, liver, lung, kidney). This advantageous feature meets the prerequisite for the detection of lymph node metastasis. In previous work, we have attempted to detect lymph node metastasis by using a macromolecule probe, poly(*N*-vinylpyrrolidone)-conjugated iridium (III) complex (Ir-PVP).[8] However, Ir-PVP needs to be administered by footpad injection and hardly accumulates in the lymph node after systemic injection (< 1 % ID/g at 4 h after intravenous injection, Figure S6), which hinders its further application. With the good delivery efficiency of Ir-CM to lymph node, diagnosis of undefined lymph node metastasis after systemic injection becomes possible, making this imaging agent very practical for further translational development and clinical applications.

The biocompatibility of Ir-CM was also evaluated. Early apoptosis, late apoptosis and necrosis of SH-SY5Y cells were measured by staining with annexin V and propidium iodide (PI) after treatment with Ir-CM for 48 h. As show in Figure S7, Ir-CM showed very low cytotoxicity at concentrations up to 8 mg mL^{-1}. After treatment with 8 mg mL^{-1} Ir-CM for 48 h and irradiation by a 595 nm light source (40 J cm^{-2}), SH-SY5Y cells still exhibit high viability (> 88 %), indicating low phototoxicity of the nanosensor (Figure S7). Serum biochemistry assessment shows no significant change in liver function related indexes, including alanine aminotransferase (ALT), alkaline phosphatase (AKP) and aspartate aminotransferase (AST), as well as kidney function related indexes, including blood urea nitrogen (BUN), creatinine (CREA) and urea (UREA), within 7 d after intravenous injection of Ir-CM (100 mg kg^{-1}), revealing the low hepatotoxicity and low renal toxicity of the nanosensor (Figure S8). Histopathological examination of different organs (heat, liver, spleen, kidney, lung) dissected from ICR mice at 7 d after intravenous injection of Ir-CM (100 mg kg^{-1}) showed that tissue morphologies of these organs were not significantly disturbed by Ir-CM treatment (Figure S9). These results indicate that the nanosensor has good biocompatibility in vitro and in vivo.

In summary, we have developed a hypoxia-activated near-infrared emitting nanosensor, Ir-CM. With this nanosensor, we are able to track cancer metastasis by non-invasive whole-body optical imaging. After intravenous injection of Ir-CM, metastasis of cancer cells to lung through the bloodstream or to the lymph node through lymphatics can be effectively detected non-invasively with high sensitivity and specificity. Ir-CM was also proven to be highly biocompatible both in vitro and in vivo. We believe the reported nanosensor provides a powerful tool for the diagnosis of cancer metastasis.

Keywords: cancer metastasis · diagnostics · hypoxia · nanosensors · optical imaging

How to cite: *Angew. Chem. Int. Ed.* **2015**, *54*, 8094 – 8099
Angew. Chem. **2015**, *127*, 8212 – 8217

[1] a) S. Valastyan, R. A. Weinberg, *Cell* **2011**, *147*, 275 – 292; b) P. S. Steeg, *Nat. Med.* **2006**, *12*, 895 – 904.
[2] a) M. Yang, E. Baranov, P. Jiang, F. X. Sun, X. M. Li, L. Li, S. Hasegawa, M. Bouvet, M. Al-Tuwaijri, T. Chishima, H. Shimada, A. R. Moossa, S. Penman, R. M. Hoffman, *Proc. Natl. Acad. Sci. USA* **2000**, *97*, 1206 – 1211; b) E. B. Voura, J. K. Jaiswal, H. Mattoussi, S. M. Simon, *Nat. Med.* **2004**, *10*, 993 – 998.
[3] a) P. Vaupel, A. Mayer, *Cancer Metastasis Rev.* **2007**, *26*, 225 – 239; b) N. C. Denko, *Nat. Rev. Cancer* **2008**, *8*, 705 – 713.
[4] J. T. Erler, K. L. Bennewith, M. Nicolau, N. Dornhöfer, C. Kong, Q. T. Le, J. T. Chi, S. S. Jeffrey, A. J. Giaccia, *Nature* **2006**, *440*, 1222 – 1226.
[5] a) K. C. Black, Y. Wang, H. P. Luehmann, X. Cai, W. Xing, B. Pang, Y. Zhao, C. S. Cutler, L. V. Wang, Y. Liu, Y. Xia, *ACS Nano* **2014**, *8*, 4385 – 4394; b) Q. Lin, C. Bao, Y. Yang, Q. Liang, D. Zhang, S. Cheng, L. Zhu, *Adv. Mater.* **2013**, *25*, 1981 – 1986.
[6] a) X. D. Wang, O. S. Wolfbeis, *Chem. Soc. Rev.* **2014**, *43*, 3666 – 3761; b) P. Babilas, G. Liebsch, V. Schacht, I. Klimant, O. S. Wolfbeis, R. M. Szeimies, C. Abels, *Microcirculation* **2005**, *12*, 477 – 487; c) A. J. Nichols, E. Roussakis, O. J. Klein, C. L. Evans, *Angew. Chem. Int. Ed.* **2014**, *53*, 3671 – 3674; *Angew. Chem.* **2014**, *126*, 3745 – 3748; d) T. Yoshihara, Y. Yamaguchi, M. Hosaka, T. Takeuchi, S. Tobita, *Angew. Chem. Int. Ed.* **2012**, *51*, 4148 – 4151; *Angew. Chem.* **2012**, *124*, 4224 – 4227; e) X. D. Wang, J. A. Stolwijk, T. Lang, M. Sperber, R. J. Meier, J. Wegener, O. S. Wolfbeis, *J. Am. Chem. Soc.* **2012**, *134*, 17011 – 17014.
[7] a) P. Babilas, V. Schacht, G. Liebsch, O. S. Wolfbeis, M. Landthaler, R. M. Szeimies, C. Abels, *Br. J. Cancer* **2003**, *88*, 1462 – 1469; b) S. Zhang, M. Hosaka, T. Yoshihara, K. Negishi, Y. Iida, S. Tobita, T. Takeuchi, *Cancer Res.* **2010**, *70*, 4490 – 4498.
[8] T. V. Esipova, A. Karagodov, J. Miller, D. F. Wilson, T. M. Busch, S. A. Vinogradov, *Anal. Chem.* **2011**, *83*, 8756 – 8765.
[9] X. Zheng, X. Wang, H. Mao, W. Wu, B. Liu, X. Jiang, *Nat. Commun.* **2015**, *6*, 5834.
[10] a) X. H. Wang, H. S. Peng, L. Yang, F. T. You, F. Teng, L. L. Hou, O. S. Wolfbeis, *Angew. Chem. Int. Ed.* **2014**, *53*, 12471 – 12475; *Angew. Chem.* **2014**, *126*, 12679 – 12683; b) S. Schreml, R. J. Meier, M. Kirschbaum, S. C. Kong, S. Gehmert, O. Felthaus, S. Küchler, J. R. Sharpe, K. Wöltje, K. T. Weiß, M. Albert, U. Seidl, J. Schröder, C. Morsczeck, L. Prantl, C. Duschl, S. F. Pedersen, M. Gosau, M. Berneburg, O. S. Wolfbeis, M. Landthaler, P. Babilas, *Theranostics* **2014**, *4*, 721 – 735; c) J. Hofmann, R. J. Meier, A. Mahnke, V. Schatz, F. Brackmann, R. Trollmann, C. Bogdan, G. Liebsch, X.-D. Wang, O. S. Wolfbeis, J. Jantsch, *Methods Appl. Fluoresc.* **2013**, *1*, 045002; d) X. D. Wang, D. E. Achatz, C. Hupf, M. Sperber, J. Wegener, S. Bange, J. M. Lupton, O. S. Wolfbeis, *Sens. Actuators B* **2013**, *188*, 257 – 262; e) X. D. Wang, J. A. Stolwijk, M. Sperber, R. J. Meier, J. Wegener, O. S. Wolfbeis, *Methods Appl. Fluoresc.* **2013**, *1*, 035002.
[11] a) S. M. Borisov, I. Klimant, *Anal. Chem.* **2007**, *79*, 7501 – 7509; b) K. Koren, S. M. Borisov, R. Saf, I. Klimant, *Eur. J. Inorg. Chem.* **2011**, 1531 – 1534.
[12] X. Zhang, M. Fryknäs, E. Hernlund, W. Fayad, A. De Milito, M. H. Olofsson, V. Gogvadze, L. Dang, S. Påhlman, L. A. Schughart, L. Rickardson, P. D'Arcy, J. Gullbo, P. Nygren, R. Larsson, S. Linder, *Nat. Commun.* **2014**, *5*, 3295.
[13] J. H. Marxsen, P. Stengel, K. Doege, P. Heikkinen, T. Jokilehto, T. Wagner, W. Jelkmann, P. Jaakkola, E. Metzen, *Biochem. J.* **2004**, *381*, 761 – 767.
[14] a) M. Nakajima, M. Takeda, M. Kobayashi, S. Suzuki, N. Ohuchi, *Cancer Sci.* **2005**, *96*, 353 – 356; b) S. Kim, Y. T. Lim, E. G. Soltesz, A. M. De Grand, J. Lee, A. Nakayama, J. A. Parker, T. Mihaljevic, R. G. Laurence, D. M. Dor, L. H. Cohn, M. G. Bawendi, J. V. Frangioni, *Nat. Biotechnol.* **2004**, *22*, 93 – 97.
[15] K. Pu, A. J. Shuhendler, J. V. Jokerst, J. Mei, S. S. Gambhir, Z. Bao, J. Rao, *Nat. Nanotechnol.* **2014**, *9*, 233 – 239.
[16] Y. Tseng, Z. Xu, K. Guley, H. Yuan, L. Huang, *Biomaterials* **2014**, *35*, 4688 – 4698.

Received: April 2, 2015
Revised: May 8, 2015
Published online: June 3, 2015

